
Forecasting the Ionosphere from Sparse GNSS Data with Temporal-Fusion Transformers

Giacomo Acciarini

Advanced Concepts Team
European Space Agency (ESA)
giacomo.acciarini@esa.int

Simone Mestici

Department of Physics
Università degli Studi di Roma Sapienza
simone.mestici@uniroma1.it

Halil S. Kelebek

Department of Engineering Science
University of Oxford
halil@robots.ox.ac.uk

Linnea M. Wolniewicz

Department of Information and Computer Science
University of Hawai'i at Mānoa
linneamw@hawaii.edu

Michael D. Vergalla

Free Flight Research Lab
mike@freeflightlab.org

Madhulika Guhathakurta

NASA Headquarters
madhulika.guhathakurta@nasa.gov

Olga Verkhoglyadova

NASA Jet Propulsion Laboratory
olga.verkhoglyadova@jpl.nasa.gov

Thomas Berger

Space Weather Technology, Research, and Education Center
University of Colorado Boulder
Thomas.Berger@colorado.edu

Bala Poduval

University of New Hampshire
balapoduval@gmail.com

Atılım Güneş Baydin

Department of Computer Science
University of Oxford, UK
gunes@robots.ox.ac.uk

Frank Soboczenski

Department of Computer Science
University of York & King's College London
frank.soboczenski@york.ac.uk

Abstract

The ionosphere critically influences Global Navigation Satellite Systems (GNSS), satellite communications, and Low Earth Orbit (LEO) operations, yet accurate prediction of its variability remains challenging due to nonlinear couplings between solar, geomagnetic, and thermospheric drivers. Total Electron Content (TEC), a key ionospheric parameter, is derived from GNSS observations, but its reliable forecasting is limited by the sparse nature of global measurements and the limited accuracy of empirical models, especially during strong space weather conditions. In this work, we present a machine learning framework for ionospheric TEC forecasting that leverages Temporal Fusion Transformers (TFT) to predict sparse ionosphere data. Our approach accommodates heterogeneous input sources, including solar irradiance, geomagnetic indices, and GNSS-derived vertical TEC, and applies pre-processing and temporal alignment strategies. Experiments spanning 2010–2024 demonstrate that the model achieves robust predictions up to 24 hours ahead, with

root mean square errors as low as 3.33 TECU. Results highlight that solar EUV irradiance provides the strongest predictive signals. Beyond forecasting accuracy, the framework offers interpretability through attention-based analysis, supporting both operational applications and scientific discovery. To encourage reproducibility and community-driven development, we release the full implementation as the open-source toolkit `ionopy`.

1 Introduction

The ionosphere, Earth’s charged atmospheric layer extending from \sim 50 to 1,000 km altitude, plays a crucial role in modern technological infrastructure and daily life [1]. This plasma layer, mainly influenced by solar radiation, magnetospheric convection and thermospheric neutral dynamics [2], directly affects critical systems including Global Navigation Satellite Systems (GNSS) accuracy, satellite communications, and Low Earth Orbit (LEO) orbital stability [3, 4]. A fundamental parameter for characterizing ionospheric behavior is the Total Electron Content (TEC), defined as the integrated electron density along a given path. TEC data are often converted to vertical TEC (vTEC) using a shell approximation and/or mapping function to account for ray path obliquity [5]. Figure 1 illustrates this process, showing slant paths from GNSS satellites projected to their vertical equivalent. Accurate vTEC prediction is essential for correcting GNSS signal delays, particularly during highly dynamic space weather events.

The Madrigal database [6], maintained by CEDAR and hosted at MIT Haystack Observatory, is among the largest repositories of upper atmospheric data. It integrates multi-decade observations from over 159 instruments, including incoherent scatter radars and GNSS-based vTEC, providing global (albeit sparse) coverage with 5-minute temporal resolution. Sparse GNSS RINEX data¹ are instead used by international research groups to generate Global Ionospheric Maps (GIM) of vTEC, like the one produced by the Jet Propulsion Laboratory (JPL) [7]. Comparing GIM products against Madrigal’s independent observations serves as a standard validation benchmark.

Despite rich observations, TEC prediction remains challenging due to nonlinear coupling between solar activity, geomagnetic conditions, and ionospheric response. Empirical models like the International Reference Ionosphere (IRI) [8, 9], though useful for climatology, show reduced accuracy during geomagnetic disturbances when ionospheric dynamics are most critical. This motivates machine learning approaches that can capture complex patterns from multi-source data.

Here, we focus on accurate ionospheric prediction by forecasting vTEC using a time-fusion transformer architecture, with the sparse GNSS Madrigal dataset serving as the target. Our framework provides a flexible benchmarking platform that supports probabilistic forecasting, heterogeneous input sources, and scientific experimentation by accommodating varying input features, time histories, and resolutions. To foster reproducibility and community-driven innovation, we publicly release our implementation as `ionopy`², offering a foundation for both applied and fundamental ionospheric research.

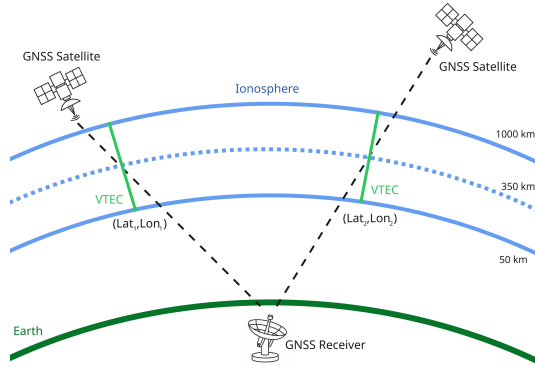


Figure 1: Schematic cross-section showing the conversion of Total Electron Content (TEC) to Vertical Total Electron Content (vTEC, green) using the Single Layer Ionospheric Model.

¹<https://cddis.nasa.gov>

²<https://github.com/spaceml-org/ionopy> , accessed 30 August 2025

2 Background

2.1 Machine Learning and Ionosphere Modeling

The application of machine learning to ionospheric modeling has gained significant momentum in recent years, driven by the limitations of traditional physics-based and empirical approaches and the increasing availability of datasets. Early studies have applied classical algorithms such as gradient boosting (XGBoost) and Multi-Layer Perceptrons (MLP) to predict the global state of the ionosphere [10, 11], while more advanced methods, such as Bi-directional Long-Term-Short-Term Memory (BiLSTM) and transformers, have shown promising results in modeling temporal dependencies, though sometimes restricted to limited geographic areas. Part of these studies have leveraged the JPL-GIM as a target data source since it provides a homogeneous set with respect to latitude and longitude [12, 13]. Instead, some of the regional forecasting models have also used the sparse GNSS-derived vTEC and demonstrated that modern ML models trained on Madrigal TEC data could significantly outperform traditional models [14, 15, 16].

The ability to ingest heterogeneous, multi-source data represents a key advantage of machine learning approaches over empirical and physics-based models. Modern ML models can potentially simultaneously incorporate solar activity indices (F10.7, sunspot numbers), geomagnetic activity parameters (Dst, Kp indices), solar wind parameters, historical TEC observations, or even SDO images, to create comprehensive predictive frameworks. This multi-modal capability is particularly important for ionospheric and thermosphere modeling, where the complex interplay between solar, magnetospheric, and thermospheric processes might require consideration of numerous input variables [17].

2.2 Temporal Fusion Transformers

We employ Temporal Fusion Transformers (TFT) [18] to forecast vTEC behavior, leveraging their state-of-the-art design for multi-horizon time series forecasting with built-in interpretability. TFT integrates specialized components such as the variable selection network, sequence-to-sequence LSTM layers to replace positional encodings, and multi-head attention to handle heterogeneous inputs and temporal patterns common in real-world forecasting.

Key features include the variable selection network, which identifies and weights relevant input features, critical for ionospheric modeling, where parameter importance varies across conditions. Moreover, static covariate encoders incorporate time-invariant factors such as location, conditioning temporal processing with geographic and seasonal/daily contexts. Finally, the sequence-to-sequence LSTM layers replace positional encoding, better capturing local trends enriched with static information. Most importantly, TFT's interpretable multi-head attention highlights influential time steps and features, offering transparent insights into relationships between solar activity, geomagnetic disturbances, and vTEC behavior.

3 Data & Methodology

In terms of input features, day-of-year, longitude, and seconds-in-day are sine/cosine encoded to preserve cyclical relationships, while other coordinates are standardized or log-normalized depending on their statistical properties. Target vTEC values are log-transformed and standardized using pre-computed statistics to address typical skewness in ionospheric measurements. The dataset was constructed from Madrigal data by selecting ten million samples with as uniform time coverage as possible over the 2010-2024 period.

The framework integrates diverse data sources with different temporal resolutions, including Thermosphere, Ionosphere, Mesosphere Energetics and Dynamics (TIMED) Solar EUV Experiment (SEE) Level 3, OMNI solar wind, indices and magnetic field data, JPLD Global Ionospheric Maps, solar activity proxies (F10.7, M10.7, S10.7, Y10.7), and geomagnetic indices (Dst, Ap). Temporal alignment and resampling are applied, followed by standardization or log-transformation for highly skewed data. JPLD data is subsampled to 10 equally spaced global points. Static features (latitude, longitude, day-of-year) and temporal features (geomagnetic and solar inputs) are aligned, normalized, and prepared for input into a TFT model.

Input datasets include NASA's OMNIWeb 1-minute high-resolution data [19], Ap index from Cestrack [20, 21], F10.7, M10.7, S10.7, Y10.7 solar proxies [22], TIMED SEE Level 3 solar irradiance

data up to 190nm at 1nm resolution [23], and JPL-GIM data³ [7]. The data was split into training (about 80%), validation (about 10%), and test (about 10%) sets following a strategy similar to that used in [12, 17]. For each year from 2010 to 2024, one month was held out for validation and another for testing, with the selected months varying across years. Care was taken to ensure that periods containing strong geomagnetic storm events were included within the validation and test sets. This split ensures that the model is evaluated on completely unseen periods of time while maintaining seasonal and solar activity representativeness, critical for maintaining accuracy to unseen space weather conditions

4 Results

Table 1 summarizes the outcomes of experiments using the Temporal Fusion Transformer (TFT) with two attention heads, two LSTM layers, a hidden state size of 64, and a 10% dropout rate. Each row of the table corresponds to a different experimental setup, where the input features, their historical time windows (lag), and temporal resolutions (res) were varied. Model performance was evaluated on a completely held-out test set spanning 2010–2024, using root mean squared error (RMSE) and mean absolute error (MAE). Both the mean (μ) and standard deviation (σ) of vTEC (in TEC units, 1 TECU = 10^{16} electrons/m²) are reported, since these values are available in the Madrigal dataset and predicted by the TFT. Prediction horizons ranged from 60 minutes up to 24 hours. In bold, the minimum errors across all experiments are reported.

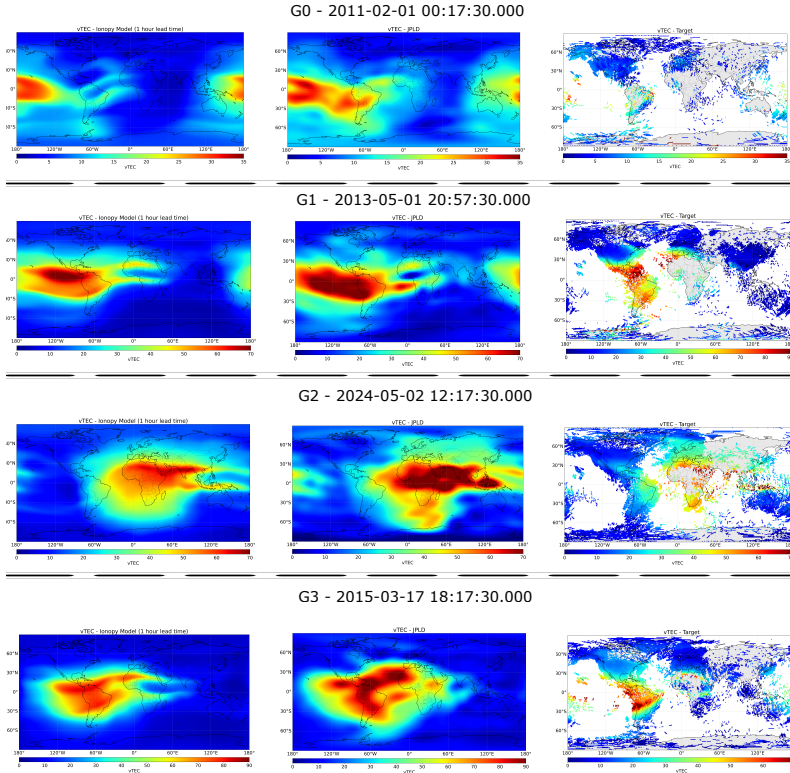


Figure 2: Results of Ionopy temporal fusion transformer model with 1 hour lead time (left column) against ground truth target vTEC data derived from GNSS (right column), and the corresponding calibrated JPL-GIM map (center column).

Overall, models that incorporated the complete set of features and utilized longer historical time windows demonstrated superior performance, as anticipated. Importantly, the results demonstrate that TIMED SEE L3 irradiance data can effectively replace traditional solar proxies, providing comparable predictive accuracy while offering direct EUV irradiance measurements. Moreover,

³https://sideshow.jpl.nasa.gov/pub/iono_daily/gim_for_research/jpld/

Table 1: Temporal fusion transformer results with different input features lags and resolutions. Metrics include mean and standard deviation for MAE and RMSE on the unseen test set.

OMNI Indices (minutes)	OMNI Solar lag, res		OMNI Magnetic Field lag, res		Ap (minutes)	Solar Proxies lag, res	TIMED SEE L3 lag, res (days)			JPL-GIM lag, res (minutes)	MAE μ, σ	RMSE μ, σ (TECU)
	Solar lag, res	Magnetic Field lag, res	lag, res	lag, res			lag, res	lag, res	lag, res			
1620, 60	1620, 60	1620, 60	27, 1	X	27, 1	X	27, 1	X	X	2.37, 0.33	3.73, 0.51	
X	X	X	81, 1	X	81, 1	X	81, 1	X	X	2.47, 0.32	3.80, 0.50	
8640, 60	8640, 60	8640, 60	144, 1	X		X		8640, 60	8640, 60	2.16, 0.32	3.38, 0.49	
8640, 60	X	8640, 60	144, 1	144, 1	X	X	8640, 60	8640, 60	8640, 60	2.16, 0.31	3.40, 0.49	
8640, 60	8640, 60	8640, 60	8640, 60	X	144, 1	X	8640, 60			2.15, 0.31	3.37, 0.49	
8640, 60	8640, 60	8640, 60	8640, 60	X		X				3.85, 0.36	5.58, 0.55	
8640, 60	8640, 60	8640, 60	8640, 60	X		X				3.47, 0.34	5.01, 0.51	
6480, 60	6480, 60	6480, 60	6480, 60	108, 1		X	108, 1			2.42, 0.33	3.81, 0.50	
3240, 60	3240, 60	3240, 60	3240, 60	54, 1		X	54, 1			2.38, 0.32	3.70, 0.50	
8100, 60	8100, 60	8100, 60	8100, 60	135, 1		X	135, 1			2.45, 0.32	3.86, 0.50	
8640, 60	8640, 60	8640, 60	8640, 60	144, 1		144, 1	144, 1			2.34, 0.32	3.67, 0.49	
4320, 60	4320, 60	4320, 60	4320, 60	72, 1		X	72, 1			2.41, 0.32	3.80, 0.50	
4860, 60	4860, 60	4860, 60	4860, 60	81, 1		X	81, 1			2.43, 0.32	3.79, 0.50	
8640, 60	8640, 60	8640, 60	8640, 60	144, 1		144, 1	X	8640, 60	8640, 60	2.17, 0.32	3.40, 0.50	
8640, 60	8640, 60	8640, 60	8640, 60	144, 1		144, 1	X			2.31, 0.31	3.60, 0.49	
X	8640, 60	8640, 60	8640, 60	144, 1		144, 1	X	8640, 60	8640, 60	2.35, 0.31	3.68, 0.49	
8640, 60	8640, 60	8640, 60	8640, 60	144, 1		144, 1	X	8640, 60	8640, 60	2.14, 0.32	3.34, 0.49	

solar irradiance seems to be the most critical input for ionospheric forecasting: when JPL-GIM data, TIMED irradiance, and solar proxies were excluded, model errors nearly doubled (up to about 5.6 TECU in RMSE for the mean). While the inclusion of JPL-GIM features provided a modest performance boost, the improvement was marginal. This suggests that EUV irradiance and geomagnetic activity alone are sufficient to enable reliable ionospheric forecasts up to one day ahead.

Figure 2 further illustrates the TFT’s predictions with a one-hour lead time (left column) compared against GNSS-derived ionospheric data (right column) under four different geomagnetic storm conditions (based on NOAA geomagnetic storm G-classes). The central column displays corresponding JPL-GIM maps (calibrated on sparse data, not predictions). Qualitatively it is confirmed that the TFT model successfully reproduces key ionospheric structures, such as the equatorial double crest enhancement (also called Equatorial Ionization Anomaly) and day–night variations during geomagnetic storm conditions.

More detailed performance metrics are provided in Appendix, where Tables 2, 3, and 4 present loss values aggregated by latitude, geomagnetic storm conditions, and solar activity levels.

5 Conclusions

In this work, we introduce and release the open-source framework `ionopy`, designed to preprocess, temporally align, and integrate solar and geomagnetic data to predict GNSS-derived sparse vTEC using Temporal Fusion Transformers. Solar EUV irradiance emerges as the most influential predictor, enabling accurate forecasts from 1 to 24 hours lead time, with RMSE as low as 3.33 TECU in the best experiments. These results highlight the potential of machine learning to outperform traditional ionospheric models and demonstrate the framework’s flexibility for testing scientific hypotheses, including the impact of varying input features, lags, and temporal resolutions.

Acknowledgments

This research is the result of the Frontier Development Lab, Heliolab a partnership between NASA, Trillium Technologies Inc. (USA), Google Cloud, NVIDIA and Pasteur Labs, Contract No. 80GSFC23CA040. A portion of research was carried out at the Jet Propulsion Laboratory, California Institute of Technology, under a contract with NASA. The authors thank Umaa Rebba Pragada and Andrew Smith for their valuable insights, NASA’s Goddard Space Flight Center, and NASA’s Jet Propulsion Laboratory for their continuing support.

References

- [1] Thomas E Berger, MJ Holzinger, EK Sutton, and JP Thayer. Flying through uncertainty. *Space Weather*, 18(1):e2019SW002373, 2020.
- [2] Michael C Kelley. *The Earth's ionosphere: Plasma physics and electrodynamics*, volume 96. Academic press, 2009.
- [3] Jr. Kintner, P. M. Observations of velocity shear driven plasma turbulence. *Journal of Geophysical Research*, 81(A28):5114–5122, October 1976.
- [4] Ryuho Kataoka, Daikou Shiota, Hitoshi Fujiwara, Hidekatsu Jin, Chihiro Tao, Hiroyuki Shinnaga, and Yasunobu Miyoshi. Unexpected space weather causing the reentry of 38 starlink satellites in february 2022. *Journal of Space Weather and Space Climate*, 12:41, 2022.
- [5] Norbert Jakowski, C Mayer, MM Hoque, and V Wilken. Total electron content models and their use in ionosphere monitoring. *Radio Science*, 46(06):1–11, 2011.
- [6] Cariglia K. Rideout W. The open madrigal initiative.
- [7] Léo Martire, Thomas F Runge, Xing Meng, Siddharth Krishnamoorthy, Panagiotis Vergados, Anthony J Mannucci, Olga P Verkhoglyadova, Attila Komjáthy, Angelyn W Moore, Robert F Meyer, et al. The jpl-gim algorithm and products: multi-gnss high-rate global mapping of total electron content. *Journal of Geodesy*, 98(5), 2024.
- [8] Dieter Bilitza, Lee-Anne McKinnell, Bodo Reinisch, and Tim Fuller-Rowell. The international reference ionosphere today and in the future. *Journal of Geodesy*, 85(12):909–920, 2011.
- [9] Dieter Bilitza, David Altadill, Vladimir Truhlik, Valentin Shubin, Ivan Galkin, Bodo Reinisch, and Xueqin Huang. International reference ionosphere 2016: From ionospheric climate to real-time weather predictions. *Space weather*, 15(2):418–429, 2017.
- [10] Aleksei V Zhukov, Yury V Yasyukevich, and Aleksei E Bykov. Gimli: Global ionospheric total electron content model based on machine learning. *GPS Solutions*, 25(1):19, 2021.
- [11] A Smirnov, Y Shprits, F Prol, H Lühr, M Berrendorf, I Zhelavskaya, and C Xiong. A novel neural network model of earth's topside ionosphere. *sci rep* 13: 1303, 2023.
- [12] O Verkhoglyadova, N Maus, and X Meng. Classification of high density regions in global ionospheric maps with neural networks. *Earth and Space Science*, 8(7):e2021EA001639, 2021.
- [13] Chung-Yu Shih, Cissi Ying-tsen Lin, Shu-Yu Lin, Cheng-Hung Yeh, Yu-Ming Huang, Feng-Nan Hwang, and Chia-Hui Chang. Forecasting of global ionosphere maps with multi-day lead time using transformer-based neural networks. *Space Weather*, 22(2):e2023SW003579, 2024.
- [14] Zhou Chen, Mingwu Jin, Yue Deng, Jing-Song Wang, Heng Huang, Xiaohua Deng, and Chun-Ming Huang. Improvement of a deep learning algorithm for total electron content maps: Image completion. *Journal of Geophysical Research: Space Physics*, 124(1):790–800, 2019.
- [15] Pan Xiong, Dulin Zhai, Cheng Long, Huiyu Zhou, Xuemin Zhang, and Xuhui Shen. Long short-term memory neural network for ionospheric total electron content content forecasting over china. *Space Weather*, 19(4):e2020SW002706, 2021.
- [16] TY Yang, JY Lu, YY Yang, YH Hao, M Wang, JY Li, and GC Wei. Gnss–vtc prediction based on cnn–gru neural network model during high solar activities. *Scientific Reports*, 15(1):9109, 2025.
- [17] Giacomo Acciarini, Edward Brown, Tom Berger, Madhulika Guhathakurta, James Parr, Christopher Bridges, and Attilim Güneş Baydin. Improving thermospheric density predictions in low-earth orbit with machine learning. *Space weather*, 22(2):e2023SW003652, 2024.
- [18] Bryan Lim, Sercan Ö Arik, Nicolas Loeff, and Tomas Pfister. Temporal fusion transformers for interpretable multi-horizon time series forecasting. *International journal of forecasting*, 37(4):1748–1764, 2021.
- [19] JH King and NE Papitashvili. Solar wind spatial scales in and comparisons of hourly wind and ace plasma and magnetic field data. *Journal of Geophysical Research: Space Physics*, 110(A2), 2005.
- [20] J Bartels. The standardized index, ks, and the planetary index, kp. *IATME bull*, 97(12b):0001, 1949.

- [21] David A Vallado and TS Kelso. Using eop and space weather data for satellite operations. *Advances in the Astronautical Sciences*, 123:2473–2493, 2006.
- [22] W Kent Tobiska, S Dave Bouwer, and Bruce R Bowman. The development of new solar indices for use in thermospheric density modeling. *Journal of Atmospheric and Solar-Terrestrial Physics*, 70(5):803–819, 2008.
- [23] Thomas N Woods, Francis G Eparvier, Scott M Bailey, Phillip C Chamberlin, Judith Lean, Gary J Rottman, Stanley C Solomon, W Kent Tobiska, and Donald L Woodraska. Solar euv experiment (see): Mission overview and first results. *Journal of Geophysical Research: Space Physics*, 110(A1), 2005.

Appendix

Table 2: TFT results for different latitude bands. Metrics include MAE and RMSE for both mean and standard deviation.

OMNI Indices (minutes)	OMNI Solar Wind lag, res (minutes)	OMNI Magnetic Field lag, res (minutes)	Ap Index (days)	Solar Proxies lag, res (days)	TIMED SEE L3 lag, res (days)	JPL-GIM lag, res (minutes)	RMSE μ, σ (TECU)
1620, 60	1620, 60	1620, 60	27, 1	X	27, 1	X	<30°: 5.663, 0.578 30–60°: 2.625, 0.407 >60°: 2.217, 0.511
X	X	X	81, 1	X	81, 1	X	<30°: 5.707, 0.570 30–60°: 2.719, 0.396 >60°: 2.338, 0.501
8640, 60	8640, 60	8640, 60	144, 1	X	X	8640, 60	<30°: 5.135, 0.568 30–60°: 2.341, 0.395 >60°: 2.100, 0.498
8640, 60	X	8640, 60	144, 1	144, 1	X	8640, 60	<30°: 5.159, 0.563 30–60°: 2.365, 0.394 >60°: 2.077, 0.496
8640, 60	8640, 60	8640, 60	X	144, 1	X	8640, 60	<30°: 5.084, 0.563 30–60°: 2.353, 0.393 >60°: 2.107, 0.494
8640, 60	8640, 60	8640, 60	X	X	X	X	<30°: 8.220, 0.620 30–60°: 4.358, 0.452 >60°: 3.216, 0.553
8640, 60	8640, 60	8640, 60	144, 1	X	X	X	<30°: 7.370, 0.590 30–60°: 3.900, 0.416 >60°: 2.945, 0.519
6480, 60	6480, 60	6480, 60	108, 1	X	108, 1	X	<30°: 5.826, 0.572 30–60°: 2.644, 0.405 >60°: 2.285, 0.497
3240, 60	3240, 60	3240, 60	54, 1	X	54, 1	X	<30°: 5.591, 0.571 30–60°: 2.643, 0.400 >60°: 2.249, 0.501
8100, 60	8100, 60	8100, 60	135, 1	X	135, 1	X	<30°: 5.893, 0.572 30–60°: 2.692, 0.399 >60°: 2.271, 0.500
8640, 60	8640, 60	8640, 60	144, 1	144, 1	144, 1	X	<30°: 5.562, 0.569 30–60°: 2.579, 0.397 >60°: 2.229, 0.496
4320, 60	4320, 60	4320, 60	72, 1	X	72, 1	X	<30°: 5.801, 0.572 30–60°: 2.640, 0.400 >60°: 2.269, 0.497
4860, 60	4860, 60	4860, 60	81, 1	X	81, 1	X	<30°: 5.756, 0.572 30–60°: 2.689, 0.403 >60°: 2.256, 0.501
8640, 60	8640, 60	8640, 60	144, 1	144, 1	X	8640, 60	<30°: 5.155, 0.574 30–60°: 2.371, 0.401 >60°: 2.106, 0.498
8640, 60	8640, 60	8640, 60	144, 1	144, 1	X	X	<30°: 5.450, 0.559 30–60°: 2.555, 0.389 >60°: 2.179, 0.491
8640, 60	8640, 60	8640, 60	144, 1	X	144, 1	X	<30°: 5.569, 0.567 30–60°: 2.594, 0.395 >60°: 2.219, 0.494
X	8640, 60	8640, 60	144, 1	144, 1	144, 1	8640, 60	<30°: 5.041, 0.561 30–60°: 2.319, 0.393 >60°: 2.093, 0.493
8640, 60	8640, 60	X	144, 1	144, 1	144, 1	8640, 60	<30°: 5.037, 0.560 30–60°: 2.335, 0.390 >60°: 2.100, 0.493

Table 3: TFT results for different geomagnetic storm conditions. Metrics include MAE and RMSE for both mean and standard deviation.

OMNI Indices (minutes)	OMNI Solar Wind lag, res (minutes)	OMNI Magnetic Field lag, res (minutes)	Ap Index lag, res (days)	Solar Proxies lag, res (days)	TIMED			RMSE μ, σ (TECU)
	L3 lag, res (days)	SEE lag, res (days)	JPL-GIM lag, res (minutes)					
1620, 60	1620, 60	1620, 60	27, 1	X	27, 1	X		Ap [0-39]: 3.64, 0.50 Ap (39-67]: 6.86, 0.76 Ap (67-111]: 8.55, 1.08 Ap (111-300]: 10.43, 0.74
								Ap [0-39]: 3.70, 0.49 Ap (39-67]: 7.94, 0.77 Ap (67-111]: 8.98, 1.13 Ap (111-300]: 11.01, 0.74
X	X	X	81, 1	X	81, 1	X		
8640, 60	8640, 60	8640, 60	144, 1	X	X	8640, 60		Ap [0-39]: 3.31, 0.49 Ap (39-67]: 6.66, 0.76 Ap (67-111]: 7.27, 1.08 Ap (111-300]: 9.28 , 0.74
								Ap [0-39]: 3.32, 0.48 Ap (39-67]: 6.72, 0.77 Ap (67-111]: 7.14 , 1.12 Ap (111-300]: 9.32, 0.73
8640, 60	X	8640, 60	144, 1	144, 1	X	8640, 60		Ap [0-39]: 3.29, 0.48 Ap (39-67]: 6.46 , 0.76 Ap (67-111]: 7.30, 1.13 Ap (111-300]: 9.34 , 0.73
8640, 60	8640, 60	8640, 60	X	144, 1	X	8640, 60		Ap [0-39]: 5.49, 0.54 Ap (39-67]: 8.74, 0.84 Ap (67-111]: 9.92, 1.19 Ap (111-300]: 12.33, 0.78
								Ap [0-39]: 4.94, 0.51 Ap (39-67]: 7.68, 0.75 Ap (67-111]: 8.35, 1.08 Ap (111-300]: 10.95, 0.74
8640, 60	8640, 60	8640, 60	144, 1	X	X	X		Ap [0-39]: 3.73, 0.49 Ap (39-67]: 7.41, 0.76 Ap (67-111]: 8.36, 1.11 Ap (111-300]: 10.45, 0.75
6480, 60	6480, 60	6480, 60	108, 1	X	108, 1	X		Ap [0-39]: 3.62, 0.49 Ap (39-67]: 7.17, 0.76 Ap (67-111]: 8.55, 1.12 Ap (111-300]: 9.91, 0.74
								Ap [0-39]: 3.77, 0.49 Ap (39-67]: 7.25, 0.77 Ap (67-111]: 8.62, 1.13 Ap (111-300]: 10.82, 0.74
3240, 60	3240, 60	3240, 60	54, 1	X	54, 1	X		Ap [0-39]: 3.59, 0.49 Ap (39-67]: 6.93, 0.76 Ap (67-111]: 8.33, 1.12 Ap (111-300]: 9.90, 0.74
								Ap [0-39]: 3.71, 0.49 Ap (39-67]: 7.47, 0.77 Ap (67-111]: 8.65, 1.12 Ap (111-300]: 9.84, 0.74
4320, 60	4320, 60	4320, 60	72, 1	X	72, 1	X		Ap [0-39]: 3.70, 0.49 Ap (39-67]: 7.21, 0.77 Ap (67-111]: 8.57, 1.12 Ap (111-300]: 9.97, 0.75
								Ap [0-39]: 3.32, 0.49 Ap (39-67]: 6.85, 0.74 Ap (67-111]: 7.38, 1.12 Ap (111-300]: 9.44, 0.74
4860, 60	4860, 60	4860, 60	81, 1	X	81, 1	X		Ap [0-39]: 3.52, 0.48 Ap (39-67]: 6.86, 0.77 Ap (67-111]: 8.42, 1.10 Ap (111-300]: 10.12, 0.73
								Ap [0-39]: 3.59, 0.49 Ap (39-67]: 7.03, 0.75 Ap (67-111]: 8.39, 1.09 Ap (111-300]: 10.10, 0.74
8640, 60	8640, 60	8640, 60	144, 1	X	144, 1	X		Ap [0-39]: 3.25 , 0.48 Ap (39-67]: 6.83, 0.78 Ap (67-111]: 7.24, 1.14 Ap (111-300]: 9.52, 0.74
								Ap [0-39]: 3.26, 0.48 Ap (39-67]: 6.64 , 0.74 Ap (67-111]: 7.31, 1.08 Ap (111-300]: 9.54, 0.74
X	8640, 60	8640, 60	144, 1	144, 1	144, 1	8640, 60		

Table 4: TFT results for different solar irradiance activity levels. Metrics include MAE and RMSE for both mean and standard deviation.

OMNI Indices (minutes)	OMNI Solar Wind lag, res (minutes)	OMNI Magnetic Field lag, res (minutes)	Ap Index lag, res (days)	Solar Proxies lag, res (days)	TIMED SEE L3 lag, res (days)	JPL-GIM lag, res (minutes)	RMSE μ, σ (TECU)
1620, 60	1620, 60	1620, 60	27, 1	X	27, 1	X	F10.7 [0-70]: 1.88, 0.28 F10.7 (70-150): 3.62, 0.53 F10.7 [150-200]: 5.73, 0.66
X	X	X	81, 1	X	81, 1	X	F10.7 [0-70]: 1.88, 0.28 F10.7 (70-150): 3.68, 0.52 F10.7 [150-200]: 5.87, 0.65
8640, 60	8640, 60	8640, 60	144, 1	X	X	8640, 60	F10.7 [0-70]: 1.72, 0.27 F10.7 (70-150): 3.28, 0.51 F10.7 [150-200]: 5.20, 0.67
8640, 60	X	8640, 60	144, 1	144, 1	X	8640, 60	F10.7 [0-70]: 1.72, 0.27 F10.7 (70-150): 3.28, 0.51 F10.7 [150-200]: 5.24, 0.66
8640, 60	8640, 60	8640, 60	X	144, 1	X	8640, 60	F10.7 [0-70]: 1.73, 0.27 F10.7 (70-150): 3.26, 0.51 F10.7 [150-200]: 5.14, 0.65
8640, 60	8640, 60	8640, 60	X	X	X	X	F10.7 [0-70]: 2.33, 0.31 F10.7 (70-150): 5.42, 0.58 F10.7 [150-200]: 8.98, 0.69
8640, 60	8640, 60	8640, 60	144, 1	X	X	X	F10.7 [0-70]: 2.12, 0.31 F10.7 (70-150): 4.95, 0.53 F10.7 [150-200]: 8.27, 0.67
6480, 60	6480, 60	6480, 60	108, 1	X	108, 1	X	F10.7 [0-70]: 1.86, 0.28 F10.7 (70-150): 3.70, 0.52 F10.7 [150-200]: 5.91, 0.66
3240, 60	3240, 60	3240, 60	54, 1	X	54, 1	X	F10.7 [0-70]: 1.87, 0.28 F10.7 (70-150): 3.59, 0.52 F10.7 [150-200]: 5.79, 0.66
8100, 60	8100, 60	8100, 60	135, 1	X	135, 1	X	F10.7 [0-70]: 1.86, 0.28 F10.7 (70-150): 3.73, 0.52 F10.7 [150-200]: 6.04, 0.65
8640, 60	8640, 60	8640, 60	144, 1	144, 1	144, 1	X	F10.7 [0-70]: 1.86, 0.28 F10.7 (70-150): 3.58, 0.52 F10.7 [150-200]: 5.60, 0.65
4320, 60	4320, 60	4320, 60	72, 1	X	72, 1	X	F10.7 [0-70]: 1.86, 0.28 F10.7 (70-150): 3.70, 0.52 F10.7 [150-200]: 5.87, 0.66
4860, 60	4860, 60	4860, 60	81, 1	X	81, 1	X	F10.7 [0-70]: 1.88, 0.28 F10.7 (70-150): 3.65, 0.52 F10.7 [150-200]: 5.97, 0.66
8640, 60	8640, 60	8640, 60	144, 1	144, 1	X	8640, 60	F10.7 [0-70]: 1.81, 0.27 F10.7 (70-150): 3.29, 0.52 F10.7 [150-200]: 5.23, 0.68
8640, 60	8640, 60	8640, 60	144, 1	144, 1	X	X	F10.7 [0-70]: 1.81, 0.27 F10.7 (70-150): 3.49, 0.51 F10.7 [150-200]: 5.56, 0.65
8640, 60	8640, 60	8640, 60	144, 1	X	144, 1	X	F10.7 [0-70]: 1.84, 0.28 F10.7 (70-150): 3.57, 0.51 F10.7 [150-200]: 5.70, 0.65
X	8640, 60	8640, 60	144, 1	144, 1	144, 1	8640, 60	F10.7 [0-70]: 1.69, 0.27 F10.7 (70-150): 3.22, 0.51 F10.7 [150-200]: 5.14, 0.65
8640, 60	8640, 60	X	144, 1	144, 1	144, 1	8640, 60	F10.7 [0-70]: 1.72, 0.27 F10.7 (70-150): 3.23, 0.51 F10.7 [150-200]: 5.12, 0.64